Fast radio-frequency amplitude modulation in multiple-quantum magic-angle-spinning nuclear magnetic resonance: Theory and experiments

P. K. Madhu and Amir Goldbourt
Department of Chemical Physics, Weizmann Institute of Science, Rehovot 76100, Israel

Lucio Frydman
Department of Chemistry, M/C 111, University of Illinois at Chicago, 845 West Taylor Street, Chicago, Illinois 60607-7061

Shimon Vega[a)]
Department of Chemical Physics, Weizmann Institute of Science, Rehovot 76100, Israel

(Received 19 August 1999; accepted 19 October 1999)

Multiple-quantum magic-angle-spinning (MQMAS NMR) spectroscopy has become a routine method to obtain high-resolution spectra of quadrupolar nuclei. One of the main problems in the performance of this experiment has been the poor efficiency of the radio-frequency pulses used in converting multiple-quantum coherences to the observable single-quantum signals. As the MQMAS experiment is basically an echo experiment this problem can be related to the efficiency with which continuous wave pulses can normally achieve the multiple- to single-quantum conversion for different crystallites in a spinning powdered sample. In this paper we investigate various aspects involved in this multiple-to-single quantum conversion, in the hope to facilitate the devise of new experimental schemes that can lead to significant MQMAS signal enhancements. We examine in particular a recently suggested experiment for MQMAS spectroscopy which employs amplitude-modulated radio-frequency pulses, and which can yield substantial signal and even resolution enhancements over the commonly used pulse schemes in MQMAS experiments. The mechanisms of operation of continuous-wave and of amplitude-modulated pulses as applied to the selective manipulation of spin-3/2 coherence elements are examined in detail, with the aid of the fictitious spin-1/2 formalism in combination with quadrupolar adiabaticity arguments. New insight into the nature of the MQMAS experiment is thus revealed, and the superior performance of suitable amplitude modulations toward the formation of MQMAS powder echoes is justified. Experimental results highlighting the utility of this scheme in samples possessing multiple quadrupolar sites with varying quadrupolar anisotropies and chemical shift offsets are demonstrated, as is the relative insensitivity of the new signal-enhancement technique to the actual level of rf irradiation. Further implications and uses of this new irradiation scheme are also briefly discussed. © *2000 American Institute of Physics.* [S0021-9606(00)00703-0]

I. INTRODUCTION

The potential applications of NMR spectroscopy to the study of materials containing quadrupolar nuclei have been well documented in a gamut of fields including inorganic chemistry, catalysis, geochemistry, and cuprate high temperature superconductivity.[1–6] These studies have been recently stimulated by the introduction of the multiple-quantum magic-angle-spinning spectroscopy (MQMAS) NMR experiment, capable of yielding high resolution spectra from half-integer quadrupolar nuclei devoid of both first- and second-order interactions.[7] This experiment averages out all anisotropic spin interactions by a combination of spatial and spin space manipulations, and at its core lies the excitation of $-m \leftrightarrow +m$ multiple-quantum coherences (MQC) and their subsequent conversion to single-quantum coherences (SQC) which are correlated in a two-dimensional (2D) fashion. Such experiment has become quite widespread due to the simplicity of its implementation, and it has enabled new applications on a variety of nuclei possessing different spin quantum numbers and coupling environments such as sodium, aluminum, rubidium, oxygen, boron, niobium, chlorine, and cobalt.[8–17]

The pulse scheme suggested for the initial MQMAS experiments has come a long way with several improvements geared at bypassing its limitations with respect to efficient excitation of MQC, of the subsequent conversion to SQC, and for obtaining spectra with purely absorptive line shapes.[18–21] Numerous studies have concentrated on analyzing the effects of spinning speed, rf power, and decoupling, on the efficiency of the MQMAS experiment.[18–25] This progress has been supplemented by the use of *z*-filtering, split-t_1 procedures, and synchronized data acquisitions.[26–29] Particularly worth mentioning in the context of the present analysis is the rotation-induced adiabatic coherence transfer (RIACT) experiment proposed by Griffin and co-workers;[29] this uses two long continuous-wave (cw) pulses for both ex-

a)Author to whom all correspondence should be addressed; electronic mail: civega@wis.weizmann.ac.il

citation and conversion of the MQC, and relies on adiabatic transfer arguments[30] to enhance quantitativeness and resolution along the multiple quantum dimension. Despite all these significant advancements in both theoretical and experimental strategies a basic problem faced by this experiment remains; namely, the relative inefficiency of the MQC→SQC conversion. One way to alleviate this problem and thereby the potentially poor signal to noise ratio of the spectra is by pushing the limits of rf power, spinning speeds, and magnetic fields used in the experiments.[31] Although this criterion is at the moment a potent driving force for the manufacture of dedicated hardware for this experiment, further progress will also demand an improved insight into the spin dynamics that occur under the relevant Hamiltonians and their relation to new pulse sequences. Contributing to such stimulus is the main goal of the present paper.

A common emphasis of the outlined investigations has been the use of rectangular pulses. Relevant literature on high resolution NMR, however, recommends the use of shaped pulses for efficient excitation in the case of spin half systems.[32] Some efforts in this direction have been made, particularly toward improving the excitation efficiency of the MQC.[33–35] The present analysis emphasizes the modulation and shaping of pulses during the efficiency-limited conversion step. In fact the possibility of using amplitude-modulated (AM) pulses for converting MQC to SQC was first examined by Vega and Naor in studies of half-integer quadrupole single crystals,[36] which showed that up to a threefold increase for the central transition signal of a spin-3/2 was possible by combining selective 90° pulses and AM rf acting as simultaneous 180° pulses on the satellites. In this class of experiments the modulation frequency of the rf could be exactly matched to the quadrupolar frequency of the nuclei in the single crystal, but these ideas have also been subsequently extended to the case of powders.[37–41] Many of these latter techniques have in common the use of frequency sweeps, which result in nearly adiabatic inversions of the satellite transitions. Two related advancements have been very recently made in the field of MQMAS spectroscopy. One of these makes use of double frequency sweeps over a large range covering the satellite transitions of all crystallites in a powder, to achieve a MQC→SQC conversion.[42] The second method replaces the conversion pulse by fast-amplitude-modulated (FAM) irradiation of the satellite transitions, and has been shown to lead to significant sensitivity enhancements on a variety of samples and under various experimental conditions.[43] A principal advantage of the latter scheme is that FAM is achieved simply by fast 180° phase shifts of the irradiating rf thereby using the built-in potentials of standard NMR spectrometers. The present paper examines the mechanism of operation of these conversion pulses. Toward this end a MQMAS formalism based on fictitious spin-1/2 operators is developed, and used to reveal new features not only of FAM-based pulse sequences but also of approaches based on usage of short cw pulses and of rotor-induced adiabatic transfers. The results of these new analytical formulations are then extensively corroborated by both numerical and experimental results, which highlight the usage of the FAM scheme toward resolution and selectivity enhancement. Furthermore, despite the technical differences between our new FAM scheme and those proposed on the basis of rf sweeps the physical phenomena involved in both of these techniques are very similar, and therefore most of the FAM arguments outlined in the following sections can be extended with only minor modifications to the case of frequency sweeps too.

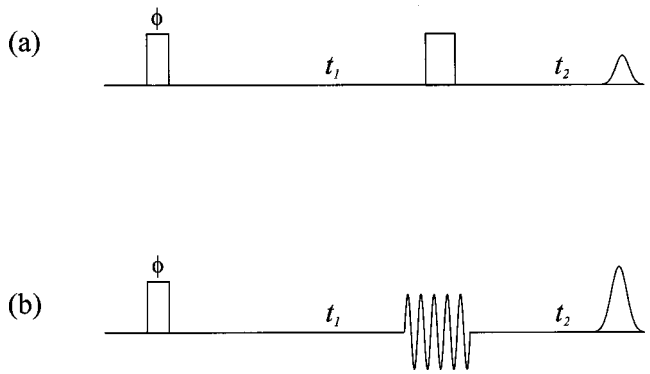

FIG. 1. (a) Basic two-pulse scheme employed in MQMAS experiments. The first pulse is phase cycled as $\phi=0°,60°,120°,180°,240°,300°$; if the second pulse is kept at a constant phase of 0° the receiver is then alternated as 0°, 180°. The TQC selected after the first pulse is converted to SQC after the second (cw) pulse and results for a powder sample in an echo along the t_2 domain due to the refocusing of all second-order quadrupolar anisotropies. (b) Generalized FAM pulse scheme; all pulse and receiver phases are cycled as in (a), but the conversion step is implemented by a symmetric irradiation of the satellite transitions within the spin manifold. Experimentally, the FAM pulse was implemented in this study via the four-point scheme $[0,\omega_1,-\omega_1,0]_n$, with each of these events lasting 1 μs and the block repeated $n=3-5$ times. The $\omega_1/-\omega_1$ modulation of the rf field strength (in kilohertz) was implemented by shifting the rf phase by 180°.

II. THEORY

A. General considerations

It is worthwhile to begin this analysis by reviewing the basic pulse sequence for MQMAS experiments [Fig. 1(a)], that is of common use and has served as a building block for many later developments in the field. The first pulse in this sequence excites all possible coherences for a given spin quantum number, and the desired order of MQC is then selected by appropriate phase cycling. This is then converted by a second pulse to observable SQ magnetization after a t_1 evolution period; an echo of the anisotropic second-order quadrupole evolution is subsequently formed at a time t_2 equal to a specific fraction of t_1 which depends on the spin quantum number and on the order of MQC that had been selected.[7] The pulse sequence that triggers the present analysis employs the FAM methodology outlined in Fig. 1(b), where the cw conversion pulse has been replaced with an amplitude-modulated profile. We have recently shown experimentally that this modification—easily carried out, for instance, by a four-point discrete modulation of the form $(\omega_1,0,-\omega_1,0)_n$—can significantly increase the efficiency of the conversion process. In this paper we describe the effects of those pulses vis-a-vis cw ones on MQMAS spin-3/2 experiments with the aid of the fictitious spin-1/2 operator formalism.[44] This expresses both nuclear spin states as well as the relevant spin Hamiltonians in terms of $\{I_\alpha^{pq}\}_{\alpha=x,y,z}$

operators, where p,q denote states $\{|1\rangle,|2\rangle,|3\rangle,|4\rangle\}$ that correspond to the energy eigenstates of the quadrupolar Hamiltonian: $|1\rangle=|3/2\rangle$, $|2\rangle=|1/2\rangle$, $|3\rangle=|-1/2\rangle$ and $|4\rangle=|-3/2\rangle$. Important properties of these operators that will be employed throughout this study are summarized in the Appendix.

Our focus is the time evolution of a density matrix which at time $t=0$ only has TQC as its elements, and which is converted to SQC by the action of either short-cw, long-cw (RIACT) or FAM pulses (Fig. 1). Higher spin systems $I \geqslant 5/2$ will be discussed at a later stage. We begin here by considering an $I=3/2$ spin in the rotating frame, whose Hamiltonian is given by[45]

$$\mathcal{H}=-\Delta\omega I_z+\tfrac{1}{6}\omega_Q[3I_z^2-I(I+1)]+3\{\omega_Q^{(2,1)}[4I(I+1)-8I_z^2-1]I_z+\omega_Q^{(2,2)}[2I(I+1)-2I_z^2-1]I_z\}+\omega_1 I_x, \tag{1}$$

where $\Delta\omega$ takes into account the resonance offset and chemical shift anisotropy (CSA) effects, ω_Q and $\omega_Q^{(2,i)}$ reflect the first- and second-order quadrupolar frequencies, and ω_1 is the rf field strength. It is convenient to present this Hamiltonian also in the language of single transition operators; in preparation for the consideration of modulated rf fields we thus rewrite Eq. (1) as

$$\mathcal{H}(t)=-\sum_{p<q}\Delta\omega^{pq}I_z^{pq}+\omega_Q(I_z^{12}-I_z^{34})+(\sqrt{3}\omega_1(I_x^{12}+I_x^{34})+2\omega_1 I_x^{23})\left(\sum_n (a_n^c\cos\omega_m t+a_n^s\sin\omega_m t)+a_0\right), \tag{2}$$

where p,q take values from 1 to 4, the $\Delta\omega^{pq}$ account for off-resonance as well as second-order quadrupolar shifts, and ω_m is the basic frequency with which the rf is potentially modulated. The condition $\Sigma_n[(a_n^c)^2+(a_n^s)^2]^{1/2}+a_0=1$ can be demanded in this expression and thus result in a general Hamiltonian which can account for the simultaneous presence of linearly polarized cw and/or FAM irradiations. Still, in the ensuing discussions and for simplicity we will deal mainly with modulations of the form $a_1\cos\omega_m t$; the cases for FAM and cw may therefore be distinguished by

$$a_0=0,\quad a_1^c=1 \quad \text{pure FAM},$$
$$a_0=1,\quad a_n=0 \quad \text{pure cw}, \tag{3}$$

and the Hamiltonian in Eq. (2) can be cast for the following discussion as

$$\mathcal{H}(t)=-(\Delta\omega^{14}I_z^{14}+\Delta\omega^{23}I_z^{23})+\omega_Q(I_z^{12}-I_z^{34})+(\sqrt{3}\omega_1(I_x^{12}+I_x^{34})+2\omega_1 I_x^{23})(a_1\cos\omega_m t+a_0). \tag{4}$$

In this expression $\Delta\omega^{23}=\Delta\omega+\omega^s(1/2)$ and $\Delta\omega^{14}=3\Delta\omega+\omega^s(3/2)$ account for both the shielding and second-order quadrupolar shifts of the central single-quantum (2–3) and of the triple-quantum (1–4) transitions, respectively. With this general Hamiltonian we shall now concentrate on the specific FAM and cw scenarios.

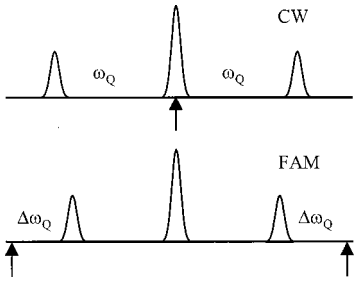

FIG. 2. Diagrammatic representation of both the cw and the FAM irradiation sequences in the rotating frame, with the arrows representing the frequencies of the irradiation fields. As in the text, $\Delta\omega_Q=\omega_Q-\omega_m$, with ω_m the modulation frequency and ω_Q the quadrupole frequency.

B. FAM Hamiltonian

As previously mentioned the basic Hamiltonian for the FAM case can be written with $a_0=0$ and $a_1=1$, i.e.,

$$\mathcal{H}(t)=-(\Delta\omega^{14}I_z^{14}+\Delta\omega^{23}I_z^{23})+\omega_Q(I_z^{12}-I_z^{34})+[\sqrt{3}\omega_1(I_x^{12}+I_x^{34})+2\omega_1 I_x^{23}]\cos\omega_m t. \tag{5}$$

The time dependence of this nutation Hamiltonian can be eliminated by transforming it into a modulated interaction frame via the propagator

$$U_m(t)=\exp[i\omega_m(I_z^{12}-I_z^{34})t]. \tag{6}$$

Transformation of $\mathcal{H}(t)$ by Eq. (6) yields

$$\mathcal{H}_m=U_m^{-1}\mathcal{H}(t)U_m=\Delta\omega_Q(I_z^{12}-I_z^{34})-(\Delta\omega^{14}I_z^{14}+\Delta\omega^{23}I_z^{23})+\frac{\sqrt{3}}{2}\omega_1(I_x^{12}+I_x^{34}), \tag{7}$$

where $\Delta\omega_Q=\omega_Q-\omega_m$ and the assumption $\omega_1\ll\omega_m$ has been made. This last approximation enables us to neglect all coefficients oscillating at frequencies ω_m and $2\omega_m$, as well as terms like $2\omega_1\cos\omega_m t I_x^{23}$. This modulated-frame Hamiltonian can also be written as

$$\mathcal{H}_m=\mathcal{H}_{12}+\mathcal{H}_{34}+\mathcal{H}^d, \tag{8}$$

where all terms commute with one another and their explicit forms are

$$\mathcal{H}_{12}=\omega_1^a I_x^{12}+\Delta^{12}I_z^{12},$$
$$\mathcal{H}_{34}=\omega_1^a I_x^{34}+\Delta^{34}I_z^{34}, \tag{9}$$
$$\mathcal{H}^d=\Delta(I_z^{14}+I_z^{23}),$$

with

$$\Delta^{12}=\Delta\omega_Q-\Delta\omega+\tfrac{1}{2}(\omega^s(\tfrac{1}{2})-\omega^s(\tfrac{3}{2})),$$
$$\Delta^{34}=-\Delta\omega_Q-\Delta\omega+\tfrac{1}{2}(\omega^s(\tfrac{1}{2})-\omega^s(\tfrac{3}{2})),$$
$$\Delta=-2\Delta\omega-\tfrac{1}{2}(\omega^s(\tfrac{1}{2})+\omega^s(\tfrac{3}{2})), \tag{10}$$
$$\omega_1^a=\frac{\sqrt{3}}{2}\omega_1.$$

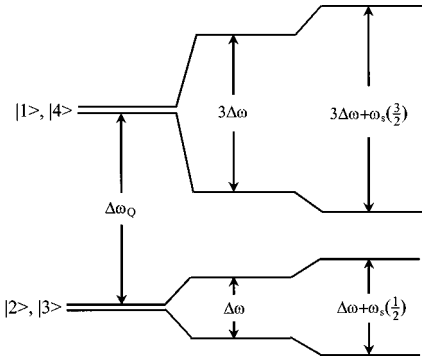

FIG. 3. Energy level diagram of a spin−3/2 nucleus subjected to FAM irradiation represented in the rotating/modulated frame. The positions of the energy levels in this frame are determined by the residual quadrupole interaction $\Delta\omega_Q=\omega_Q-\omega_m$ and by the chemical shift and second-order quadrupolar shift terms in $\Delta\omega$. Also depicted are the evolution frequencies of triple (1–4) and single (2–3) quantum coherences, given by $\Delta\omega^{23}=\Delta\omega+\omega^s(1/2)$ and $\Delta\omega^{14}=3\Delta\omega+\omega^s(3/2)$, respectively.

Both $\mathcal{H}_{12}$ and $\mathcal{H}_{34}$ look like conventional spin-1/2 nutation Hamiltonians, while $\mathcal{H}^d$ is purely diagonal. Thus it can be stated that a characteristic of the FAM irradiation is that by focusing on simultaneous manipulations of the satellite transitions, it transforms a complex spin-3/2 nutation manifold [Eq. (2)] into two decoupled two-level systems. Figure 2 shows this diagrammatically by comparing the principal positions of rf irradiation for both the cw and FAM cases in the rotating frame. Figure 3 on the other hand shows the energy level diagram of the FAM Hamiltonian [Eq. (8)] in the rotating/modulated frame, along with its various single-and triple-quantum transition frequencies for a system affected by potential off-resonance and second-order quadrupolar shifts. It is worth mentioning in passing that if instead of the cosine modulation we would have chosen in Eq. (5) a sine modulation of the form $(\sqrt{3}\omega_1(I_x^{12}+I_x^{34})+2\omega_1 I_x^{23})\sin\omega_m t$, the last (rf) term in Eq. (7) would have become $(\sqrt{3}/2)\omega_1(I_y^{12}-I_y^{34})$. Still, the important subspace-decoupling characteristic of the FAM irradiation would naturally have been preserved.

A point of interest of these transformations into a modulated frame is the way by which they allow us to calculate analytically the time dependence of the density matrix coefficients during the pulse. Indeed the density matrix in this new frame can be written as

$$\rho_m(t)=U_m^{-1}(t)\rho U_m(t)=\sum_i\sum_{p<q}a_i^{pq}(t)I_i^{pq}, \tag{11}$$

where ρ is the density matrix in the rotating frame and i takes the indices x,y and z. Hence, since

$$\begin{aligned}\rho_m^{23}&=\rho^{23},\\ \rho_m^{14}&=\rho^{14},\end{aligned} \tag{12}$$

(where as usual the superscripts 23 and 14 correspond to the blocks of the density matrix characterizing the $1/2\leftrightarrow-1/2$ and $3/2\leftrightarrow3/2$ transitions), the values of both the single- and the triple-quantum coherences are independent of whether the rotating or rotating/modulated frames are chosen for the MQMAS description.

As indicated earlier our interest deals with the effects of the second, MQ conversion pulse. Within an $I=3/2$ framework we thus discuss the time evolution of a TQC given by an initial density matrix of the form $\rho_0=a_xI_x^{14}+a_yI_y^{14}$, acted under the effects of the Hamiltonian given in Eq. (8). We will be particularly interested in the conversion process of these coherences into $I_{x,y}^{23}$, a spin dynamics that can be represented as

$$\begin{aligned}I_x^{14}&\rightarrow c_{xx}(t)I_x^{23}+c_{xy}(t)I_y^{23},\\ I_y^{14}&\rightarrow c_{yy}(t)I_y^{23}+c_{yx}(t)I_x^{23}.\end{aligned} \tag{13}$$

The time-dependent nutation coefficients c_{xx} and c_{xy} represent the ''amounts'' of I_x^{23} and I_y^{23} created from I_x^{14}, while c_{yy} and c_{yx} represent the ''amounts'' of I_y^{23} and I_x^{23} created from I_y^{14}. Much of the focus in the discussion to follow will be on the values and relative signs adopted by these coefficients in the FAM and cw cases, the importance of which will become evident during the presentation. For the sake of clarity we begin by exploring their behavior in static and spinning FAM cases, beginning with the former.

1. FAM-driven conversions in static single crystals

The simplest scenario to consider pertains to nonspinning single crystals, as these involve single and time-independent quadrupole interactions. Furthermore if we consider the simplest possible case, which neglects all second-order quadrupolar and off-resonance shifts and sets the modulation rate of the rf such that $\omega_Q=\omega_m$ (i.e., $\Delta^{12}=\Delta^{34}=\Delta=0$), the Hamiltonian in Eq. (8) reduces simply to

$$\mathcal{H}=\omega_1^aI_x^{12}+\omega_1^aI_x^{34}. \tag{14}$$

Then according to Eq. (11), an initial density matrix given by

$$\rho_0=I_{x,y}^{14} \tag{15}$$

evolves under the action of such Hamiltonian as

$$\rho_0\rightarrow\rho(t)=I_{x,y}^{14}\cos^2\left(\frac{\omega_1^at}{2}\right)+I_{x,y}^{23}\sin^2\left(\frac{\omega_1^at}{2}\right)+\cdots, \tag{16}$$

where we have ignored all nonrelevant terms of the form $I_{x,y}^{12}$, $I_{x,y}^{13}$, $I_{x,y}^{24}$, and $I_{x,y}^{34}$. The appropriate commutation relations used to arrive at Eq. (16) are outlined in the Appendix. It is clear that in this simple approximation, starting with I_x^{14} or I_y^{14} as the initial density matrix one gets only $c_{xx}(t)I_x^{23}$ or $c_{yy}(t)I_y^{23}$. In other words, the TQC upon conversion yields pure SQC without the intermixing of the x and y terms. This does not, however, guarantee the full conversion of $I_x^{14}\rightarrow I_x^{23}$ or $I_y^{14}\rightarrow I_y^{23}$, and one can expect a loss in the amplitude of the final value taken by the SQC unless the pulse is optimized for that particular single-crystal orientation. In the case of Eq. (16) it may be noted that $c_{xx}(t)=c_{yy}(t)=\sin^2(\omega_1^at/2)$, meaning that the ''amounts'' of I_x^{23} and I_y^{23} achievable from I_x^{14} and I_y^{14} will be of the same magnitude.

Having discussed this illustrative but special case it is possible to progress into the most general static situation, involving the evolution of the initial density matrix under a general time-independent Hamiltonian with $\Delta^{12}\neq0$, $\Delta^{34}\neq0$. We are thus interested in the evolution of $I_{x,y}^{14}$ under a Hamiltonian possessing both second-order quadrupolar and

off-resonance shifts. We begin by inspecting the dynamics under the actions of $\mathcal{H}_{12}+\mathcal{H}_{34}$, a problem that can still be treated as involving two spin-1/2 cases since both of these Hamiltonians commute. Furthermore, we are only interested in following the terms:

$$\begin{aligned}\langle I_{x,y}^{14}\rangle &= \mathrm{Tr}(I_{x,y}^{14}U^{-1}I_{x,y}^{14}U),\\ \langle I_{x,y}^{23}\rangle &= \mathrm{Tr}(I_{x,y}^{23}U^{-1}I_{x,y}^{14}U).\end{aligned} \tag{17}$$

Thus with $U=U_{12}U_{34}$ and $U_{ij}=\exp(i\mathcal{H}_{ij}t)$ the terms of interest are matrix elements such as ρ_{23}, given by

$$\begin{aligned}\rho_{23}(t) &= \langle 2|\rho|3\rangle\\ &= (\langle 3|\rho|2\rangle)^*\\ &= \langle 2|U^{-1}I_{x,y}^{14}U|3\rangle\\ &\equiv \sum_{m,n}\langle 2|U^{-1}|m\rangle\langle m|I_{x,y}^{14}|n\rangle\langle n|U|3\rangle\\ &\equiv \langle 2|U^{-1}|1\rangle\langle 1|I_{x,y}^{14}|4\rangle\langle 4|U|3\rangle\\ &\quad +\langle 2|U^{-1}|4\rangle\langle 4|I_{x,y}^{14}|1\rangle\langle 1|U|3\rangle.\end{aligned} \tag{18}$$

The second term in the last line of Eq. (18) drops out because of U's block nature; hence the only remaining term of interest is

$$\langle 2|U^{12}I_{x,y}^{14}U^{43}|3\rangle = m_{x,y}\langle 2|U^{12}|1\rangle\langle 3|U^{43}|4\rangle, \tag{19}$$

where $m_x=1/2$ and $m_y=-i/2$. Following a similar procedure for the computation of ρ_{14} [see Appendix A] a straightforward calculation yields for the time evolution of the TQC $I_{x,y}^{14}$,

$$\begin{aligned}I_{x,y}^{14}\rightarrow I_{x,y}^{14}\cos\left(\frac{\omega_1^{12}}{2}t\right)\cos\left(\frac{\omega_1^{34}}{2}t\right)+I_{x,y}^{23}\cos\alpha^{12}\cos\alpha^{34}\\ \times\sin\left(\frac{\omega_1^{12}}{2}t\right)\sin\left(\frac{\omega_1^{34}}{2}t\right)+\cdots,\end{aligned} \tag{20}$$

where we have focused again only on the $I_{x,y}^{14}$ and $I_{x,y}^{23}$ coefficients, and

$$\begin{aligned}\omega_1^{12} &= \sqrt{(\omega_1^a)^2+(\Delta^{12})^2},\\ \omega_1^{34} &= \sqrt{(\omega_1^a)^2+(\Delta^{34})^2},\\ \tan\alpha^{12} &= \frac{\Delta^{12}}{\omega_1^a},\\ \tan\alpha^{34} &= \frac{\Delta^{34}}{\omega_1^a}\end{aligned} \tag{21}$$

[the various terms appearing in Eq. (21) had been explicitly defined in Eq. (10)]. With this expression for the TQC evolution in hand it is simple now to take into account also the commuting diagonal offset term $\mathcal{H}^d=\Delta(I_z^{14}+I_z^{23})$, Eq. (20) only needs to be modified as

$$\begin{aligned}I_{x,y}^{14}\rightarrow\cos\left(\frac{\omega_1^{12}}{2}t\right)\cos\left(\frac{\omega_1^{34}}{2}t\right)[I_{x,y}^{14}\cos\Delta t\pm I_{y,x}^{14}\sin\Delta t]\\ +\cos\alpha^{12}\cos\alpha^{34}\sin\left(\frac{\omega_1^{12}}{2}t\right)\sin\left(\frac{\omega_1^{34}}{2}t\right)\\ \times[I_{x,y}^{23}\cos\Delta t\pm I_{y,x}^{23}\sin\Delta t]+\cdots.\end{aligned} \tag{22}$$

The $\cos\alpha^{ij}$ terms represent rotations in the 12 and 34 subblocks associated with TQC→SQC conversions; the maximum conversion efficiency ($\alpha=0$) is evidently obtained in the on-resonance FAM scenario $\Delta\omega_Q=0$, $\Delta=0$. Also interesting to note is the fact that because of $\mathcal{H}^d$ there is a definite passage of I_x^{14} to both I_x^{23} and I_y^{23}, unlike the special case previously considered [Eq. (16)]. This intermixing of x and y components is brought about only by the presence of chemical shifts and second-order quadrupolar couplings, but not due to the FAM off-resonance term $\omega_Q-\omega_m$.

2. FAM-driven conversions in spinning single crystals

We discuss now the evolution of an initial TQC matrix under the action of a quadrupolar Hamiltonian that has been rendered oscillatory time dependent by the action of MAS. Emphasis is again placed at this stage on the TQC→SQC conversion pathway of a single crystallite. In this case one can identify a variety of different situations depending on the initial conditions of the density matrix, and on the time dependencies of both $\omega_Q(t)$ and of the modulated rf. A key factor that will affect the conversion efficiency in both the cw and FAM pulse sequences will be the manner by which the spin system will go through the spinning-induced crossing conditions ($\Delta\omega_Q=0$ for FAM, or $\omega_Q=0$ for cw/RIACT). These crossing and anticrossing phenomena that can occur between the energy levels of a quadrupolar spin manifold being acted by rf, are best understood on the basis of adiabaticity arguments introduced by Vega.[30] These were initially established for the sake of clarifying spin-lock and cross-polarization processes in half-integer quadrupoles, where it was shown that spin states could remain locked in the initial eigenstates of the Hamiltonian (sudden passage), transform themselves into different eigenstates in a continuous fashion (adiabatic passage), or become distributed over all populations and coherences (intermediate passage).[46] Since this initial example these concepts have been used to better understand numerous other experiments including TRAPDOR,[47,48] REAPDOR,[49] MQMAS RIACT[29,50] and double frequency quadrupole sweeps.[42] As will be shown in the following the concept of adiabaticity can also provide insight into the fate of spins when $\Delta\omega_Q$ (for FAM MQMAS) or ω_Q (for cw-RIACT) decrease in a more or less sudden fashion to zero while in the presence of rf irradiation.

a. FAM evolution under an adiabatic passage. We begin the MAS discussion by restricting $\Delta^{12}(t)=-\Delta^{34}(t)$; a case that demands all off-resonance and second-order quadrupolar terms in Eqs. (8)–(10) to be neglected. To examine the effects of level crossings we will also assume that these materialize around the middle of the pulse. Starting far from the point of crossing implies that the FAM Hamiltonian at $t=0$ takes the form

$$H(t)|_{t=0}=\Delta\omega_Q(I_z^{12}-I_z^{34})+\omega_1^a(I_x^{12}+I_x^{34})$$
$$\equiv\frac{1}{2}\begin{pmatrix}\Delta\omega_Q & \omega_1^a & 0 & 0\\ \omega_1^a & -\Delta\omega_Q & 0 & 0\\ 0 & 0 & -\Delta\omega_Q & \omega_1^a\\ 0 & 0 & \omega_1^a & \Delta\omega_Q\end{pmatrix}. \quad (23)$$

Then, as long as $\Delta\omega_Q \gg \omega_1$, it is clear that the $I_{x,y}^{14}$ and $I_{x,y}^{23}$ terms of the density matrix will not be influenced by the rf. As earlier it is of interest to look into the time evolution of a density matrix whose initial form is $I_{x,y}^{14}$; for clarity we describe the evolution of each of these quadrature components separately. In order to relate the $I_{x,y}^{14}\rightarrow I_{x,y}^{23}$ conversion and the adiabaticity arguments, it is also convenient to go to a reference frame where coherences look like populations; i.e., into a system where spins are locked with respect to the Hamiltonian. With this in mind we transform I_x^{14} to a representation where it takes the form I_z^{14} at time $t=0$; this may be done with the transformation

$$U=\exp\left(-\frac{i\pi I_y^{14}}{2}\right)\exp\left(\frac{i\pi I_y^{23}}{2}\right). \quad (24)$$

It can then be verified that in this tilted frame

$$(I_x^{14})^T=I_z^{14},\quad (I_x^{23})^T=-I_z^{23} \quad (25)$$

as desired. The initial density matrix in this new tilted frame can also be written as

$$\rho_0^T=(I_x^{14})^T=I_z^{14}=\frac{1}{2}(I_z^{13}+I_z^{24}+I_z^{14}-I_z^{23}). \quad (26)$$

Under such tilting transformation the Hamiltonian in Eq. (23) becomes

$$\mathcal{H}^T(t)=\Delta\omega_Q(I_z^{13}-I_z^{24})+\omega_1^a(I_x^{13}-I_x^{24})$$
$$\equiv\frac{1}{2}\begin{pmatrix}\Delta\omega_Q & 0 & \omega_1^a & 0\\ 0 & -\Delta\omega_Q & 0 & -\omega_1^a\\ \omega_1^a & 0 & -\Delta\omega_Q & 0\\ 0 & -\omega_1^a & 0 & \Delta\omega_Q\end{pmatrix}. \quad (27)$$

$\mathcal{H}^T(t)$ can also be written in a generalized form as

$$\mathcal{H}^T(t)=\mathcal{H}_{13}+\mathcal{H}_{24}, \quad (28)$$

where we have combined the 1–3 and the 2–4 subblocks in Eq. (27). Since these two subspaces commute with one another the whole problem can again be treated as that of two uncoupled spin-1/2 systems.

As the time-dependent $\mathcal{H}^T(t)$ evolves toward a state with $\Delta\omega_Q(t)=0$ both subspaces experience an anticrossing, and an adiabatic transfer process may result. In terms of the partial populations described in Eq. (26) this will evidently be associated with the inversions

$$I_z^{13}\rightarrow -I_z^{13},\quad I_z^{24}\rightarrow -I_z^{24}. \quad (29)$$

The remaining term $I_z^{14}-I_z^{23}$ in Eq. (26) remains invariant, as can be demonstrated using the commutation relations outlined in the Appendix. After a completely adiabatic process the density matrix thus takes the form

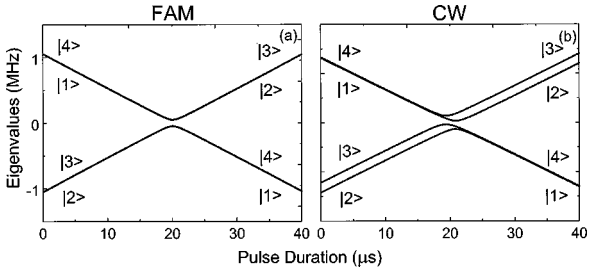

FIG. 4. Plot of the anticrossings experienced by a single crystal in FAM (a) and in cw-RIACT (b) cases as a function of the length of the pulse. While the FAM process is shown in the rotating/modulated frame, RIACT is shown in the rotating frame. These plots were done for a single crystal assuming a rf strength of 100 kHz, a quadrupole frequency (at $t=0$) of 2.4 MHz, and a zero asymmetry parameter. No second-order quadrupolar or off-resonance effects were taken into account.

$$\rho^T(t)=\tfrac{1}{2}(-I_z^{13}-I_z^{24}+I_z^{14}-I_z^{23})=-I_z^{23}. \quad (30)$$

Transformation of this $-I_z^{23}$ state from the tilted frame and back to the original modulated frame results in I_x^{23}. Hence for the case of a spinning FAM experiment an ideal adiabatic transformation will convert I_x^{14} entirely into I_x^{23}, and such conversion will take place due to level anticrossings in the 1–3, 2–4 subspaces of the modulated/tilted frame. Although this entire transfer mechanism involves only spin coherences, it is interesting to note how it can still be cast into states that are suitably spin locked and as passages that are adiabatic.

To consider now the spinning sample dynamics of the quadrature I_y^{14} state we follow the same path as before except that we rewrite the tilting operator [Eq. (24)] as

$$U=\exp\left(-\frac{i\pi I_x^{14}}{2}\right)\exp\left(\frac{i\pi I_x^{23}}{2}\right). \quad (31)$$

This transformation, which is done again to facilitate the visualization of the adiabatic process, leads to tilted states

$$(I_y^{14})^T=I_z^{14},\quad (I_y^{23})^T=I_z^{23}. \quad (32)$$

The explicit form of the tilted Hamiltonian is then

$$\mathcal{H}^T(t)=\Delta\omega_Q(I_z^{13}-I_z^{24})+\omega_1^a(I_y^{13}-I_y^{24})$$
$$\equiv\frac{1}{2}\begin{pmatrix}\Delta\omega_Q & 0 & -i\omega_1^a & 0\\ 0 & -\Delta\omega_Q & 0 & i\omega_1^a\\ i\omega_1^a & 0 & -\Delta\omega_Q & 0\\ 0 & -i\omega_1^a & 0 & \Delta\omega_Q\end{pmatrix} \quad (33)$$

and can be written in a generalized form as

$$\mathcal{H}^T(t)=\mathcal{H}_{13}+\mathcal{H}_{24}. \quad (34)$$

Transforming the initial density matrix into this new reference frame leads to

$$\rho_0^T=(I_y^{14})^T=-I_z^{14}=-\tfrac{1}{2}(I_z^{13}+I_z^{24}+I_z^{14}-I_z^{23}). \quad (35)$$

Due to the arguments given earlier it follows that an adiabatic anticrossing at $\Delta\omega_Q(t)=0$ process results in a complete population inversion, which in the case of Eq. (35) involves the simultaneous negation of both I_z^{13} and I_z^{24}. As a result we get at the conclusion of the passage

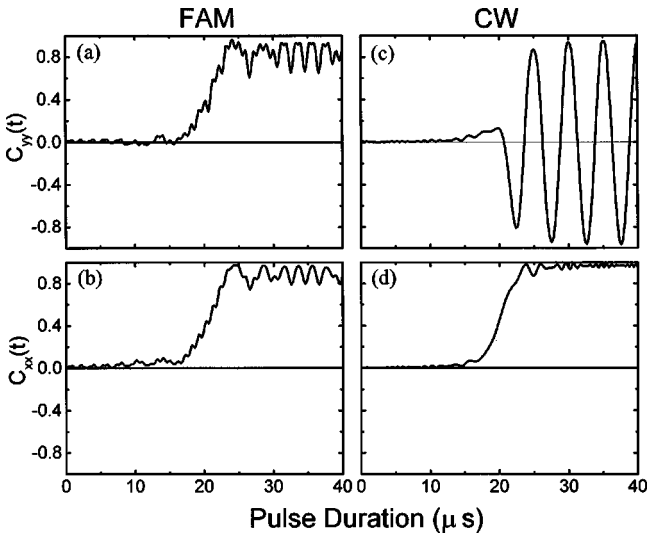

FIG. 5. Generation of SQC ($I_{x,y}^{23}$) from TQC ($I_{x,y}^{14}$) for FAM (left-hand column) and cw (right) pulse schemes. These calculations were performed on the basis of a single crystal evolution obeying Eq. (13), for which an anticrossing occurs at 20 μs. Interesting to note is the fate of the coherences during and after the anticrossings shown in Fig. 4: while no major oscillations happen in the FAM situation, $I_y^{14}\rightarrow I_y^{23}$ shows a clear oscillation in the cw case due to the presence of the rf field. These nutations persist even in the absence of second-order quadrupolar shifts. A Larmor frequency of 79.1 MHz (^{23}Na at a magnetic field of 7 T) and MAS at 6500 Hz were used for the simulations; other details are as given in Fig. 4.

$$\rho^T(t)=-\tfrac{1}{2}(-I_z^{13}-I_z^{24}+I_z^{14}-I_z^{23})=I_z^{23}, \tag{36}$$

a state which when expressed in the original modulated frame equals I_y^{23}. Hence an adiabatic process converts I_y^{14} to I_z^{23}, and here again the transfer is via coherences.

Notice that in these adiabatic cases the conversions happen as $I_x^{14}\rightarrow I_x^{23}$ and $I_y^{14}\rightarrow I_y^{23}$, with no intermixing or oscillatory behavior for either the x or the y components of the coherences. Both of these processes may thus be represented as illustrated in Fig. 4(a), where a simplified linear slope for the time dependence of the quadrupole

$$\Delta\omega_Q(t)=a_s t+\tfrac{1}{2}\Delta\omega_Q(0). \tag{37}$$

has been assumed. It may be mentioned in passing that these conversion processes cease to be ideal once off-resonance and second-order terms are introduced. Then, transfers from I_x^{14} and I_y^{14} to both I_x^{23} and I_y^{23} may result. However, as long as one works in the limit of short irradiation or of small off-resonance values the above-mentioned arguments hold true and can be relied on for meaningful conclusions.

b. FAM evolution under nonadiabatic passages. The nonadiabatic regime includes numerous scenarios: sudden anticrossing of energy levels, no anticrossing at all, and intermediate anticrossings. During the first and second of these cases and unless off-resonance and second-order quadrupolar effects are taken into consideration, nothing happens to the $I_{x,y}^{14}$ density matrix elements. In the intermediate case and again without taking into account the off-resonance and second-order quadrupolar shifts, numerical simulations point to the conclusion that transfers occur according to

$$\begin{aligned} I_x^{14}&\rightarrow c_{xx}(t)I_x^{23},\\ I_y^{14}&\rightarrow c_{yy}(t)I_y^{23}, \end{aligned} \tag{38}$$

with no intermixing or oscillatory behavior of the x and y components being observed [Figs. 5(a) and 5(b)]. Therefore it can be concluded that in general the conversion of TQC into SQC by FAM pulses occurs in a pure fashion, by which it is meant that the prefactors $c_{xx}(t)$ and $c_{yy}(t)$ are always positive, similar in magnitude, and that no $x-y$ mixing occurs. This does not imply that the efficiency of the conversion is complete, especially in the nonadiabatic case, but it means that no net rotations of the coherences in the $x-y$ plane are originated by the conversion. The important implications of this behavior with regards to the resolution and sensitivity of MQMAS experiments will become clear in the powder sample discussion. Finally, it is worth concluding by restating that if instead of the purely cosinusoidal modulation [Eq. (5)] one adopts a sinusoidal one, straightforward calculations yield exactly the same results as those presented in this paragraph.

C. cw Hamiltonian

Having treated the FAM scheme we now concentrate on the effects of cw pulses, simpler to apply experimentally but perhaps conceptually more challenging to understand and sensitivity-wise less efficient. We follow for this analysis the same line of arguments as previously mentioned (inspect the conversion pathways of both $I_{x,y}^{14}$ coherences to the respective $I_{x,y}^{23}$ elements) and then compare these results with those of FAM.

The cw Hamiltonian can be obtained from Eq. (2) by replacing it with $a_n=0$ and $a_0=1$, and can be written in terms of fictitious spin-1/2 operators as

$$\begin{aligned} \mathcal{H}=&(\omega_1^a I_x^{12}+\Delta^{12}I_z^{12})+(\omega_1^a I_x^{34}+\Delta^{34}I_z^{34})+\Delta(I_z^{14}+I_z^{23})\\ &+2\omega_1 I_x^{23}, \end{aligned} \tag{39}$$

where now the following definitions hold good:

$$\begin{aligned} \Delta^{12}&=\omega_Q-\Delta\omega+\tfrac{1}{2}(\omega^s(\tfrac{1}{2})-\omega^s(\tfrac{3}{2})),\\ \Delta^{34}&=-\omega_Q-\Delta\omega+\tfrac{1}{2}(\omega^s(\tfrac{1}{2})-\omega^s(\tfrac{3}{2})),\\ \Delta&=-2\Delta\omega-\tfrac{1}{2}(\omega^s(\tfrac{1}{2})+\omega^s(\tfrac{3}{2})),\\ \omega_1^a&=\sqrt{3}\omega_1. \end{aligned} \tag{40}$$

Neglecting the off-resonance and second-order quadrupolar terms the above Hamiltonian can be simplified into

$$\begin{aligned} \mathcal{H}&=\omega_Q(I_z^{12}-I_z^{34})+\omega_1^a(I_x^{12}+I_x^{34})+2\omega_1 I_x^{23}\\ &\equiv\frac{1}{2}\begin{pmatrix} \omega_Q & \omega_1^a & 0 & 0\\ \omega_1^a & -\omega_Q & 2\omega_1 & 0\\ 0 & 2\omega_1 & -\omega_Q & \omega_1^a\\ 0 & 0 & \omega_1^a & \omega_Q \end{pmatrix}. \end{aligned} \tag{41}$$

This matrix is to be contrasted with a static FAM Hamiltonian like that given in Eq. (23). Its main difference lies in the presence of ω_1 terms in the off-diagonal central transition positions which prevent an otherwise block diagonal

form; we clarify in the following how the presence of these terms complicates the dynamics of the TQC→SQC cw conversions.

1. cw-driven conversions in static single crystals

In analogy with the FAM case we begin by considering static single crystals with time-independent quadrupole frequencies ω_Q. Also as before, we are interested in the TQC/SQC interconversion starting from an initial density matrix of the form $\rho(0)=I_{x,y}^{14}$. After neglecting all off-resonance and second-order quadrupolar shifts the cw Hamiltonian [Eq. (39)] can be diagonalized analytically by a unitary transformation of the form

$$U=U_y^{24}(\theta_2)U_y^{13}(\theta_1)U_y^{14}\left(-\frac{\pi}{2}\right)U_y^{23}\left(\frac{\pi}{2}\right)$$
$$=\exp(i\theta_2 I_y^{24})\exp(i\theta_2 I_y^{13})\exp\left[i\frac{\pi}{2}(I_y^{14}-I_y^{23})\right]. \quad (42)$$

The Hamiltonian under the action of $U_y^{14}(-\pi/2)U_y^{23}(\pi/2)$ becomes

$$\mathcal{H}=[\omega_Q I_z^{13}+\omega_1^a I_x^{13}]-[\omega_Q I_z^{24}+\omega_1^a I_x^{24}]-2\omega_1 I_z^{23}$$
$$\equiv\frac{1}{2}\begin{pmatrix}\omega_Q & 0 & \omega_1^a & 0\\ 0 & -\omega_Q-2\omega_1 & 0 & -\omega_1^a\\ \omega_1^a & 0 & -\omega_Q+2\omega_1 & 0\\ 0 & -\omega_1^a & 0 & \omega_Q\end{pmatrix} \quad (43)$$

with the definitions

$$\omega^{13,24}=\sqrt{(\pm\omega_1-\omega_Q)^2+(\omega_1^a)^2},$$
$$\tan\theta_{12,34}=\frac{-\omega_1^a}{\pm\omega_1-\omega_{Q1}}. \quad (44)$$

Under the $U_y^{24}(\theta_2)U_y^{13}(\theta_1)$ transformation the Hamiltonian given in Eq. (43) becomes

$$\mathcal{H}^T=\omega_e^{13}I_z^{13}-\omega_e^{24}I_z^{24}+\omega_1(I_z^{12}+I_z^{34})\equiv\mathcal{H}_{13}+\mathcal{H}_{24}+\mathcal{H}^d, \quad (45)$$

which as for FAM is again given by the sum of three mutually commuting terms.

As before we consider the fates pertaining to the evolution of I_x^{14} and I_y^{14}. To treat the dynamics of an initial density matrix of the form I_x^{14} we first transform this state into the representation in which the cw Hamiltonian was made diagonal, then propagate it in this space and finally backtransform. This cumulative transformation may be represented as

$$U\exp(-i\mathcal{H}^T t)U^{-1}I_x^{14}U\exp(i\mathcal{H}^T t)U^{-1}, \quad (46)$$

where U and $\mathcal{H}^T$ are given by Eqs. (42) and (45), respectively. A straightforward calculation yields

$$I_x^{14}\rightarrow I_x^{14}\tfrac{1}{4}\{\sin^2(\theta_1)[\cos(\omega^{13}t)-1]+\sin^2(\theta_2)[\cos(\omega^{24}t)-1]+4\}+I_x^{23}\tfrac{1}{4}\{\sin^2(\theta_1)[\cos(\omega^{13}t)-1]+\sin^2(\theta_2)\times[\cos(\omega^{24}t)-1]\}+\cdots, \quad (47)$$

where again we have restricted ourselves to the coefficients of the relevant terms $I_{x,y}^{14}$ and $I_{x,y}^{23}$. It follows from this analytical calculation that starting from I_x^{14} and in the absence of offsets the coefficient of the term I_y^{23} is zero: one ends up without creating any y magnetization.

To treat the dynamics of an initial density matrix of the form I_y^{14} we do a transformation analogous to that in Eq. (46):

$$U\exp(-i\mathcal{H}^T t)U^{-1}I_y^{14}U\exp(i\mathcal{H}^T t)U^{-1}. \quad (48)$$

A straightforward calculation then yields

$$I_y^{14}\rightarrow\tfrac{1}{2}I_y^{14}\{\cos^2(\theta_1)\cos^2(\theta_2)\cos(\omega^{14}t)+\cos^2(\theta_1)\times\sin^2(\theta_2)\cos(\omega^{12}t)+\sin^2(\theta_1)\cos^2(\theta_2)\cos(\omega^{34}t)+\sin^2(\theta_1)\sin^2(\theta_2)\cos(\omega^{23}t)+\tfrac{1}{2}I_y^{23}\{\sin(\theta_1)\sin(\theta_2)\cos(\theta_1)\cos(\theta_2)(\cos\omega^{12}t-\cos\omega^{14}t+\cos\omega^{23}t-\cos\omega^{34}t)\}+\cdots. \quad (49)$$

The ω^{ij}'s in Eq. (49) are defined as

$$\omega^{12}=\omega_1+\tfrac{1}{2}(\omega^{13}+\omega^{24}),$$
$$\omega^{14}=\omega_1+\tfrac{1}{2}(\omega^{13}-\omega^{24}),$$
$$\omega^{23}=\omega_1-\tfrac{1}{2}(\omega^{13}+\omega^{24}), \quad (50)$$
$$\omega^{34}=\omega_1-\tfrac{1}{2}(\omega^{13}-\omega^{24}).$$

As before we confined ourselves only to coefficients of the $I_{x,y}^{14}$ and $I_{x,y}^{23}$ terms. It follows from this analytical calculation that the coefficient of the I_x^{23} term is zero and hence neither is in this case any intermixing of x and y components. But it is important to note that according to Eqs. (47) and (49) the ''amounts'' of I_x^{23} and I_y^{23} magnetization that can be respectively created from I_x^{14} and I_y^{14} are very different. This is in contrast to the FAM situation where the respective coefficients were equal in magnitude, and marks an important difference between the FAM and cw experiments whose consequences will become evident when dealing with powdered samples.

2. cw evolution in spinning single crystals

We turn now to the MAS case and consider a time-dependent $\omega_Q(t)$, with the relevant Hamiltonian for this case still given formally by Eq. (39). The relevance of this case lies mainly in connection to the RIACT experiment, where the conversion pulse lasts an appreciable fraction of a rotor cycle. Like before we begin by considering the evolution of $\rho_0=I_x^{14}$, and to further exploit the adiabaticity arguments introduced in the FAM paragraph we resort to solving the cw propagation with the aid of the $I_x^{14}\rightarrow I_z^{14}$ tilting transformation given in Eq. (24). The extra term in the cw Hamiltonian transforms into $-2\omega_1 I_z^{23}$, which can also be written as $-\omega_1(I_z^{13}+I_z^{24}-I_z^{14}+I_z^{23})$. Therefore, the resulting cw Hamiltonian in the tilted frame can be written as

$$\mathcal{H}^T=[(\omega_Q-\omega_1)I_z^{13}+\omega_1 I_x^{12}]-[(\omega_Q+\omega_1)I_z^{24}+\omega_1 I_x^{24}] - \omega_1(I_z^{23}-I_z^{14}) \equiv \begin{pmatrix} \omega_Q & 0 & \omega_1^a & 0 \\ 0 & -\omega_Q-2\omega_1 & 0 & -\omega_1^a \\ \omega_1^a & 0 & -\omega_Q+2\omega_1 & 0 \\ 0 & -\omega_1^a & 0 & \omega_Q \end{pmatrix}. \quad (51)$$

Hence the Hamiltonian in this case can still be written in a blocked form as $\mathcal{H}_{13}+\mathcal{H}_{24}+\mathcal{H}^d$. Furthermore, since the extra $2\omega_1 I_z^{23}$ term commutes with $(I_x^{14})^T=I_z^{14}$, the adiabatic dynamics of this state retain the same forms as they adopted in the FAM situation. The cw analogies of Eqs. (26) and (30) then are

$$\rho_0^T=(I_x^{14})^T=I_z^{14}=\tfrac{1}{2}(I_z^{13}+I_z^{24}+I_z^{14}-I_z^{23}),$$
$$\rho^T(t)=\tfrac{1}{2}(-I_z^{13}-I_z^{24}+I_z^{14}-I_z^{23})\equiv -I_z^{23}. \quad (52)$$

The second of these equations is the result of two complete adiabatic processes $I_z^{13}\rightarrow -I_z^{13}$ and $I_z^{24}\rightarrow -I_z^{24}$. Upon back-transformation from the tilted frame the resulting terms become I_x^{23}; hence it may again be seen that as in the FAM case *x*-phase TQC becomes *x*-phase SQC with unity efficiency, and no quadrature components result. The case of nonadiabatic evolution can also be treated as in the case of FAM but it will not be further detailed here; it is sufficient to state that according to numerical simulations and at least in the absence of offsets, this case will neither lead to quadrature components nor to severe oscillation during the $I_x^{14}\rightarrow I_x^{23}$ conversion.

By contrast to what happened in the FAM experiment, however, the cw nutation dynamics of the I_y^{14} term is radically different from the one just described for I_x^{14}. This happens in spite of the fact that the tilted Hamiltonian remains the same [Eq. (51)], and its origin can be traced to the fact that I_y^{14} remains invariant under the tilting transformations in Eq. (42). Indeed for all the cases considered until now the initial state $\rho(0)$ was spin-locked such that $[\rho(0),\mathcal{H}(t=0)]=0$ and even though time dependent, the Hamiltonian could always be written as the sum of two decoupled spin-1/2 interactions plus a commuting term. This allowed us to describe the fate of the coherences in terms of populations, which by adiabatic or nonadiabatic processes were inverted in suitably tilted frames resulting in effective interconversions between TQC and SQC. In the case of I_y^{14}, however, the spin system starts spin locked but during the anticrossing process it ends up connecting the two independent subspaces; its evolution is consequently no longer describable by population inversion processes. In fact these spinning-induced anticrossings in combination with the cw irradiation create coherences whose behavior is highly unpredictable, as it depends on the conditions in which both the system and the Hamiltonian are residing at time zero. This variability results in nontrivial oscillations during the $I_y^{14}\rightarrow c_{yy}(t)I_y^{23}$ conversion process, as can be clearly seen in the distinct cw transfer curves shown in Fig. 5c.

As a summary of these spinning single crystal analyses on the TQC→SQC conversion we find both analytically and numerically that for either FAM or cw irradiations $I_x^{14}\rightarrow c_{xx}(t)I_x^{23}$. But in the cw-driven $I_y^{14}\rightarrow I_y^{23}$ transfer strong oscillations set in that affect considerably the efficiency of the conversion process. Also to be noticed is the fact that while the coefficients of the $I_x^{14}\rightarrow I_x^{23}$ and $I_y^{14}\rightarrow I_y^{23}$ conversions are similar in magnitude for FAM this ceases to be true for the cw case. The consequences of these features will become clear in Sec. II D, which extends these single crystals arguments to the analysis of powdered samples.

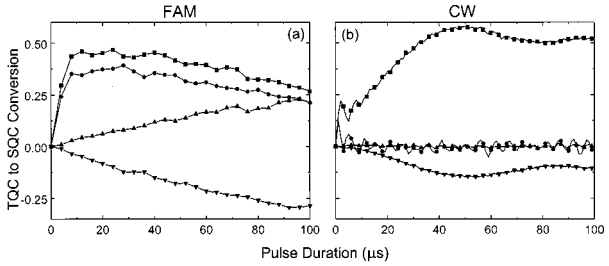

FIG. 6. Description of the triple- to single-quantum coherence conversion as a function of the pulse length for FAM (a) and cw (b) irradiations. These simulations are the result of a powder average over 3722 orientations, with second-order quadrupolar shifts but no off-resonance effects. For both (a) and (b) squares correspond to $I_x^{14}\rightarrow I_x^{23}$, circles to $I_y^{14}\rightarrow I_y^{23}$, lower triangles to $I_x^{14}\rightarrow I_y^{23}$, and upper triangles to $I_y^{14}\rightarrow I_x^{23}$. Although the conversion profiles of the last two processes start growing in the FAM situation due to the presence of second-order quadrupolar shifts, it should be remembered that normal FAM pulses are ~12–20 μs long and thus hardly affected by this phenomenon. Other simulation details are as given in Figs. 4 and 5.

D. FAM, cw, and RIACT evolution in spinning powders

Figure 6 compares the FAM versus the cw creation of SQC from TQC as a function of the conversion pulse for the case of a powder. As can be appreciated from these calculations the routine short-pulse cw schemes yield a smaller amount of SQC than FAM while in the RIACT case, where the cw conversion pulse can be as long as a quarter of a rotor cycle ($\tau_r/4$), the amount of SQC created is comparable to that of an optimized FAM pulse. Experimentally, however, we have observed that the RIACT enhancement is consistently smaller than that of FAM; we dwell in this section on explaining the reasons for this behavior.

As stated, MQMAS NMR spectroscopy is an echo experiment in which the TQC evolution during t_1 is refocused during the SQC acquisition time t_2. When fulfilling the refocusing of the second-order quadrupolar anisotropy by means of this TQC/SQC correlation, the ratio between t_1 and t_2 needs to be given for all the crystallites in the sample by

$$\frac{t_2}{t_1}=-\frac{C_4^S(1/2)}{C_4^S(3/2)}=k. \quad (53)$$

Here the $C_4^S(m)$ are orientation-independent coefficients depending only on the spin number *S* and the coherence order *m*, which have been described elsewhere in detail.[7,18] Hence, all arguments that revolve around enhancing the sensitivity of MQMAS experiments should also address the manner in which they affect the basic features of this echo formation. We consequently focus here on describing the differences among the FAM, short-pulse cw, and cw-RIACT schemes, vis-a-vis the TQC/SQC echo formation in powders.

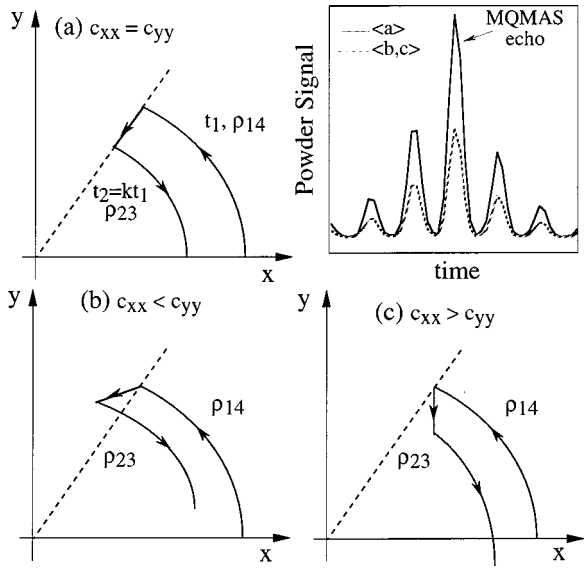

FIG. 7. Interplay between the relative magnitudes of the TQC→SQC conversion coefficients (c_{xx}, c_{yy}) and the potential attenuation of the MQMAS powder NMR echo. (a) Ideal scenario involving $|c_{xx}| = |c_{yy}|$ and showing a complete t_2 refocusing of the anisotropic second-order evolution experienced by ρ_{14} according to Eq. (53). (b), (c) Imperfect refocusing caused by unequal conversion coefficients ($|c_{xx}| \neq |c_{yy}|$); the time reversal for each crystallite is not ideal in these cases leading to overall attenuated powder echo intensities.

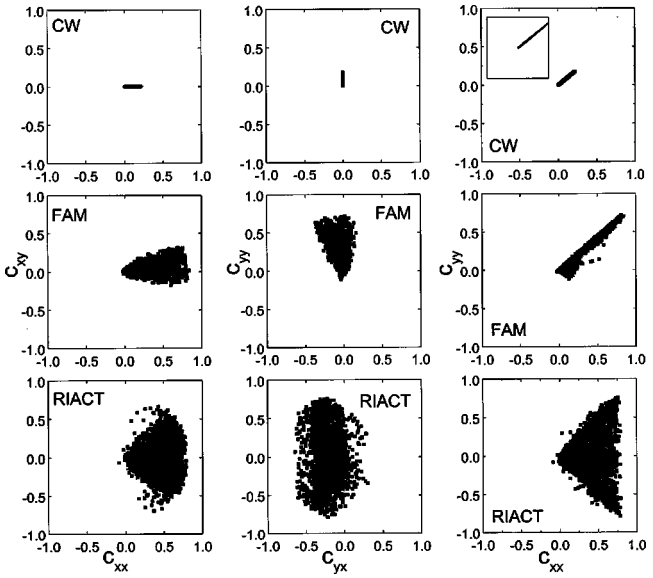

FIG. 8. Plots depicting the interdependencies of the ($c_{xx}, c_{xy}, c_{yx}, c_{yy}$) factors defining the TQC→SQC conversion in MQMAS NMR [Eq. (13)]. Each point in the plot represents the signal arising from a single crystallite belonging to the powder sample; 3722 orientations weighted by their corresponding solid angles and other simulation details as given in Figs. 4 and 5 were assumed. The top row corresponds to the short-pulse cw case, the middle one corresponds to FAM, and the bottom one to the RIACT sequence. In the c_{xx} vs c_{yy} column deviations from a slope of 1 are in detriment of the formation of an appropriate echo signal (Fig. 7); the deviations occurring even for the short-pulse cw case are highlighted by the square inset. Notice in this correlation the spread of c_{yy} to both positive and negative values upon employing RIACT as a consequence of the fast oscillations introduced in Fig. 5. By contrast, the spread for FAM is minor and originates in second-order quadrupolar shifts.

For simplicity we will assume the most straightforward variant of MQMAS experiments, one which begins by exciting the TQC of various crystallites and then lets them evolve according to their own respective second-order quadrupolar anisotropies. After an evolution time t_1 and before the application of the conversion pulse the relevant density matrix for each of the crystallites has the form

$$\rho(t_1) = a_x I_x^{14} + a_y I_y^{14}, \tag{54}$$

where for brevity we have dropped the t_1 time dependence of the a coefficients. It follows from all the previous discussions in this paper that the effect of the TQC→SQC conversion pulse can be fairly accurately summarized for either the cw, FAM, or RIACT cases as

$$\begin{aligned} a_x I_x^{14} &\rightarrow a_x c_{xx}(t) I_x^{23}, \\ a_y I_y^{14} &\rightarrow a_y c_{yy}(t) I_y^{23}. \end{aligned} \tag{55}$$

Until now most MQMAS analyses have equated improving the efficiency of a particular pulse strategy with maximizing the magnitudes of the c_{xx}, c_{yy} conversion coefficients. Also important, however, is ensuring that the absolute values of these conversion coefficients be made equal. Indeed as is schematically illustrated in Fig. 7, if a conversion sequence were to distort the relative sizes of the (c_{xx}, c_{yy}) prefactors a net orientation-dependent rotation in the $x-y$ plane would result and the refocusing condition stated by Eq. (53) would not be simultaneously attainable for all crystallites in the powder. Therefore in addition to maximizing the conversion factors, important conditions which an efficient conversion pulse scheme must satisfy should include

$$\begin{aligned} c_{xx}(t) &= \pm c_{yy}(t), \\ c_{xy}(t) &= c_{yx}(t) = 0. \end{aligned} \tag{56}$$

Here the explicit choice in sign will depend on the relative sign of the k in Eq. (53): when $k<0$ $c_{xx} = c_{yy}$ results in the inversion of the second-order quadrupolar shift, whereas when $k>0$ a reflection of the coherence is necessary to yield an echo. In the parlance of coherence transfer diagrams, the former condition corresponds to a $-3 \rightarrow -1$ pathway selection and the latter to a $+3 \rightarrow -1$ one.[7]

It is in connection with these arguments that the $c_{xx}(t) = c_{yy}(t)$ condition satisfied for the FAM but not for the cw (or RIACT) case becomes pertinent. In particular, the strong orientation dependence and oscillatory character of the $I_y^{14} \rightarrow I_y^{23}$ cw conversion process (Fig. 5) will significantly reduce the intensity of the MQMAS echo, even if single-crystal conversions are themselves efficient. In order to further clarify how the rf-induced mixing and/or oscillatory behavior of the x and y components will affect the MQMAS signals we present Fig. 8, which shows the relative sizes of all conversion prefactors for the cw (short-pulse), cw-RIACT, and FAM cases. The plots depict the creation of SQC from an ideal TQC state with $a_x = a_y = 1$ [Eq. (54)], and these calculations included second-order quadrupole effects in order to investigate their influence on the ideal behavior of each of the pulse schemes. The left-hand column of Fig. 8 shows plots of c_{xx} against c_{xy} for each of the sequences; these should have ideally been lines parallel to the $+x$ axis as c_{xy} should be null for a pure echo [Eq. (56)]. Their spread in

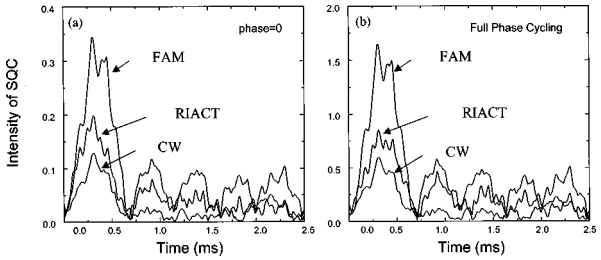

FIG. 9. (a) Comparison between the TQ/SQ MAS powder intensity echoes produced by short-pulse cw, RIACT, and FAM irradiations. These numerical simulations assumed an interpulse delay between the first and second pulse $t_1=461.5\,\mu$s (three rotor periods); the lengths of the conversion pulses were 2 μs, 41 μs (rotor period/4), and 20 μs ($n=5$) for the short-pulse, RIACT, and FAM schemes, respectively. The first pulse was assumed 7 μs long and with a relative phase of 0; therefore it only created TQCs proportional to I_x^{14}. (b) Comparison between the TQ/SQ MAS echoes produced by RIACT and FAM for similar systems and conditions as in (a), except for the fact that the phase of the first pulse was scanned over the six 0°–300° values that ϕ adopts during the actual phase cycling (Fig. 1).

the FAM and RIACT peaks is solely due to second-order quadrupolar effects; the short-pulse cw case is essentially ideal reflecting the better behavior of the system in this linear regime (but notice the much smaller c_{xx} values associated to overall weaker signals). The middle column shows similar plots of c_{yy} against c_{yx}; here again FAM performs best, as it shows an enhanced intensity with respect to the ideal cw response and a narrower distribution than RIACT. The response of FAM would have been ideal without second-order quadrupolar effects, a situation which would not have been met by RIACT due to the strong oscillations in its $I_y^{14}\rightarrow I_y^{23}$ conversion process. Yet the most important plots to be noted are those in the right-hand column, where c_{xx} is plotted with respect to c_{yy}. Ideally one would expect here a straight line of slope $+1$ as dictated by Eq. (56). A slight deviation from this slope is seen in the cw case due to $c_{xx}\neq c_{yy}$ [Eqs. (47) and (49)], while the much larger values shown by the FAM coefficients and their nearly perfect identity slope clarify the sensitivity and resolution enhancements of FAM-MQMAS as compared to cw-MQMAS. The oscillations introduced in Fig. 5 make the above picture very complicated for RIACT, explaining the attenuation of the overall powder echo signal that we have observed. From all of this we can conclude that for the short-pulse cw case we could get a nearly pure MQMAS echo but one with a low magnitude of intensity, whereas for the RIACT case the single-crystal magnitudes look promising but the powdered echo is attenuated due to oscillations in the $I_y^{14}\rightarrow I_y^{23}$ conversion. FAM, on the other hand, combines good magnitude and refocusing characteristics, and is thus a good alternative to obtain a powder MQMAS echo. Furthermore, since second-order quadrupolar effects decrease with increasing magnetic field the spread among the coefficients seen in the FAM case is expected to decrease when operating at higher fields, whereas the RIACT problems would still persist since the oscillations arise due to the rf field itself.

Figure 9 exemplifies further the relevance of these powder refocusing arguments by showing a numerical comparison between the TQ/SQ t_2 echo formation for the short-pulse cw, the cw-RIACT, and the FAM schemes. The simulations presented in part (a) assumed an I_x^{14} state as the initial condition prior to the conversion as well as typical coupling and MAS parameters, and they show a substantial advantage of the FAM over cw or RIACT schemes compared to the naive calculations shown in Fig. 6. In fact in the actual experiment, due to the cycling of the phase ϕ involved in the initial TQC coherence excitation, the FAM advantages are even larger. Indeed in these cases TQC components along both x and the y directions will be present at the time of the conversion even in the absence of any t_1 evolution. Realistic preconversion states should then read $\rho_0=I_x^{14}\cos\phi+I_y^{14}\sin\phi$, meaning that the conversion will no longer involve a pure I_x^{14} situation. Figures 7 and 8 forecast then an even stronger echo attenuation of the MQMAS RIACT echo due to the strong I_y oscillations. This scenario is reflected in Fig. 9(b), which compares both the FAM and RIACT t_2 responses that can be expected on using the actual phase cycling of an experiment involving six excitation pulses that are evenly phase shifted between 0° and 300°.

Before concluding this theoretical treatment it is worth connecting it with another feature which we have consistently observed in the FAM experiments; namely, an increase in the resolution of the MQMAS spectra along the isotropic dimension. This heuristic advantage of the FAM methodology can be traced to the relation between the better defined echoes afforded by FAM for crystallites throughout the powder, and a reduction in the peaks' mixed-phase dispersive artifacts.

III. EXPERIMENTAL PROCEDURES AND RESULTS

A. Acquisition details

A series of experiments were carried out to extend our previous observations on the usefulness of FAM MQMAS NMR,[43] as well as to further corroborate the physical insight provided by the theory of the preceding paragraphs. All of these experiments were performed in a Bruker DSX-300 MHz spectrometer equipped with a 4 mm MAS probe. The acquisitions were done mostly on ^{23}Na (a spin-3/2) with samples spinning at rates of 12 kHz; other experimental parameters included 96 kHz rf fields, $256\,t_1$ increments, 25μs t_1 increments, 12 scans per t_1 increment, the States acquisition mode,[51] and 2 s relaxation delays. The first (excitation) pulse was set at a 4.8 μs duration; the second (amplitude-modulated) pulse consisted of five consecutive blocks of the four-point modulation scheme $[0,\omega_1,-\omega_1,0]$, with each of these levels lasting for 1 μs. Programs provided by Bruker were used for the processing transformation to get the sheared MQMAS spectra. No decoupling was used during the acquisition of any of the samples. To inspect the performance of the FAM sequence on higher spin systems experiments were also performed on α-Al_2O_3 by observing at the resonance of ^{27}Al (a spin- 5/2). The first pulse used in this case had a 3 μs duration, the number of blocks employed in the FAM sequence were three, and other conditions were as stated for the spin-3/2 cases.

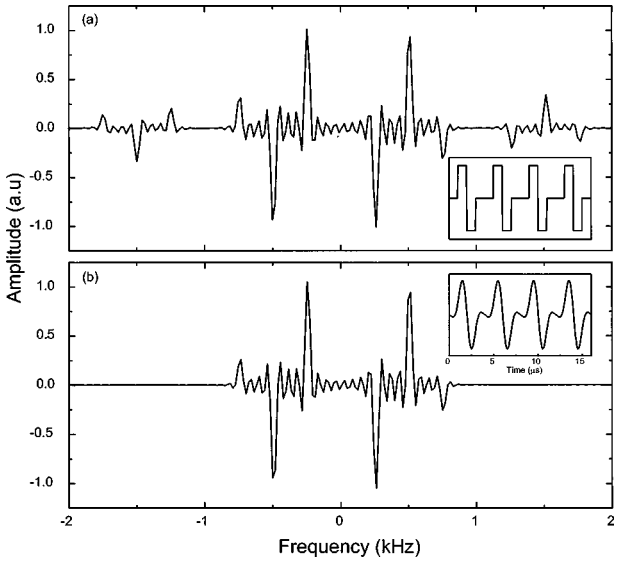

FIG. 10. Comparisons between the time domain profiles and Fourier components of (a) the four-point FAM sequence employed experimentally, and (b) a purely sinusoidal FAM of the form $\frac{2}{3}[(\sin(\omega_m t)-\sin(2\omega_m t)]$ with $\omega_m = 250$ kHz.

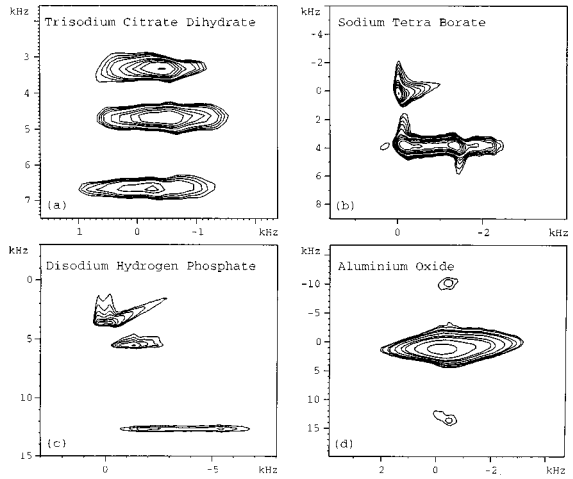

FIG. 12. Sheared two-dimensional MQMAS NMR spectra of (a) trisodium citrate dihydrate, (b) tetrasodium borate, (c) disodium hydrogen phosphate, and (d) aluminum oxide. All spectra were acquired on a DSX-300 MHz spectrometer with a rf power of 96 kHz and MAS at 12 kHz. Additional parameters for the ^{23}Na experiments [(a)–(c)] were 256 t_1 increments with 25 μs dwells, 12 scans per t_1 point, 2 s recycle delay, a first pulse of 4.8 μs duration, and a FAM pulse with n value of 5. For the aluminum sample 128 t_1 increments with 10 μs dwells, 6 scans per t_1 point, 0.5 s recycle delays, 3 μs excitation pulse widths, and FAM with $n=3$ was used.

B. Experimental FAM sequence: Frequency components

The arguments of our theoretical analysis considered only ideal cosinusoidal modes of modulation for describing the FAM sequences. Yet as was just mentioned, the actual experiments relied on the four-point modulation form $[0,\omega_1,-\omega_1,0]_n$ [Fig. 10(a), inset]. This form was chosen because of its good performance and easy implementation, as it is based on simple 180° phase shifts rather than on continuous fast amplitude changes that may be challenging to follow by high-power nonlinear electronics. We briefly dwell here on an analysis of how such choice based on the use of square phase-shifted pulses reflected on the spins' evolution. As illustrated by the Fourier component analysis shown in Fig. 10, the effects of the pulse shape that was chosen can be approximated very closely by those of a pure sine modulation of the form $\frac{2}{3}[(\sin(\omega_m t)-\sin(2\omega_m t)]$. The frequency components for both of these schemes are very similar: Apart from minor high-frequency components and for FAM levels lasting 1 μs, both irradiation schemes are dominated by peaks positioned at ± 250 and ± 500 kHz. This fact distinguishes in one important respect our experiments from the theoretical discussions presented so far, which were based on symmetric but monochromatic modulations at $\pm\omega_m$. For short experimental pulses the spins are still likely to experience, as in the ideal treatment, MAS-driven anticrossings through only one of these components. However sequential events correspond to two-level anticrossings ($|\omega_Q-\omega_m|=0$ and $|\omega_Q-2\omega_m|=0$, $\omega_m=250$ kHz) are also conceivable for the case of the double modulation. To shed further light on the qualitative behavior of spins under these conditions Fig. 11 illustrates for the case of a sinusoidal double modulation, the anticrossings exhibited by an individual crystallite across either the ω_m or $2\omega_m$ frequencies, along with the resulting buildups of its observable signal. These and other cases that we have analyzed reveal that enhancements of the signal (i.e., TQC→SQC conversions) will occur with each anticrossing in the experiment. This in turn implies that in such doubly modulated FAM sequences a larger number of crystallites will undergo anticrossing per unit time than, for instance, in a single modulated FAM or in cw cases (where crossings occur only at zero frequency). All this is reasonable by virtue of the $\omega_1 \ll \omega_m$ assumption, which implies that the overall evolution of the spins can be described by individual single-mode FAM responses. Still it should be noted that these anticrossings can also take place at different rates (differing adiabaticity parameters), thereby contributing to the signal generation in unequal ways. But in general we have observed both numerically and experimentally that the main difference between the use of ideal FAM pulses versus

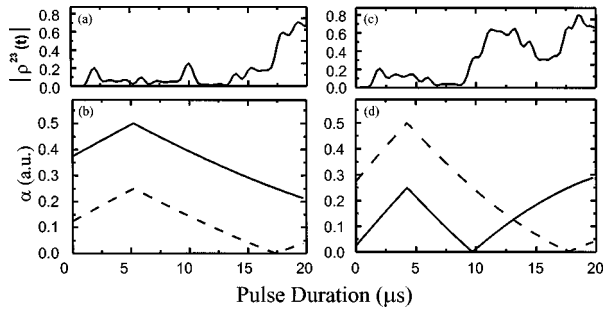

FIG. 11. Plots comparing anticrossing and conversion behaviors for the FAM sequence depicted in Fig. 10(b). The bottom plots [(b), (d)] illustrate the anticrossing parameter $\alpha=|1-\omega_q/\omega_m|$ for the two frequency irradiation components: 250 kHz (solid line) and 500 kHz (dashed line). The top traces [(a), (c)] depict the concurrent fate of the SQC (ρ_{23}) starting from an ideal TQC (ρ_{14}) of unity. Whenever an anticrossing happens ($\alpha=0$) a buildup in SQC occurs: (b) shows only one anticrossing for the 500 kHz component; plot (d) shows anticrossings for both the 250 and 500 kHz components.

TABLE I. The quadrupolar parameters and occupancy ratios of the various sites of different sodium samples.

Name of the compound	Site	$\frac{e^2qQ}{h}$	η	δ_{iso}	Site population theory	Site population FAM
Trisodium citrate dihydrate	I	1.11	0.8	−3.3	1	1
	II	1.65	0.6	1.3	1	1
	III	1.75	0.6	7	1	0.9
Disodium hydrogen phosphate	I	1.31	0.2	4.5	1	1
	II	2.04	0.7	3.4	1	0.8
	III	3.84	0.3	8.8	2	0.75
Sodium tetra borate	I	0.58	0.0	10.7	1	0.85
	II	0.92	0.2	−1.3	1	1

the use of their discrete doubly modulated counterparts is that the latter can in principle be made shorter for the same rotor spinning speeds due to the increased numbers of anticrossings. For the present study such pulse length optimization was done empirically.

C. Experimental FAM NMR results

Purposes of this paragraph include comparing the utility of FAM vis-à-vis our theoretical predictions, demonstrate its applicability to higher spin systems, illustrate its potential quantitative characteristics, and explore its offset and rf level performances. Toward these ends three different sodium samples (disodium hydrogen phosphate, tetrasodium borate and trisodium citrate dihydrate) were analyzed, as was a sample of Al_2O_3. The resulting FAM MQMAS spectra are shown in Fig. 12. The site population analysis obtained from peak integrations of the three sodium samples is outlined in Table I. There is a very good agreement with the crystallographic expectations except for the case of disodium hydrogen phosphate, for which a better matching was reported when using RIACT.[8] This is probably attributable to the use of a higher magnetic field in this previous study (14 T as against our 7 T system); indeed subsequent RIACT work done by Lim and Gray at 8.4 T[50] does not report such close agreement between theory and experiment. Hence it may be concluded that FAM sequences can be used for an acceptable estimate of site quantification, provided it is used with caution and in conjunction with information obtained from normal MAS data.[18]

From the above-mentioned theoretical discussions it is evident that all the pulse sequences aiming at improving the conversion efficiency may suffer potential offset dependencies. But because it offers the possibility of undergoing anticrossing-mediated TQC→SQC conversions at numerous positions, the operational bandwidth for the sequence in Fig. 10(a) can be expected to surpass the conversion performance of other alternatives. Indeed Fig. 13 shows the offset dependence that we observed for the experimental FAM sequence; it describes the intensity variations observed for the three sodium resonances of disodium hydrogen phosphate, and shows an overall offset behavior that is fairly robust. We also investigated experimentally the influence of the rf power on the performance of the modulation pulses. Although this parameter has been shown to exert dramatic effects on the efficiency of cw-based conversions,[22] its FAM dependence is quite different. Figure 14 shows the MQMAS echo intensities observed in a sample of sodium sulfate for the same experimental conditions previously described but as a func-

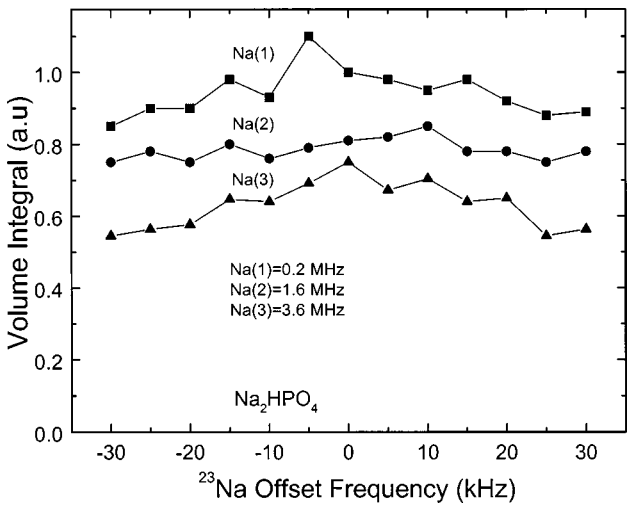

FIG. 13. Plot showing the 2D volume integral of the three sodium sites in disodium hydrogen phosphate, as extracted from a series of ^{23}Na MQMAS spectra acquired with different off-resonance values. Other experimental factors are as given in Fig. 12; the quadrupole coupling constants of each of the sites are mentioned.

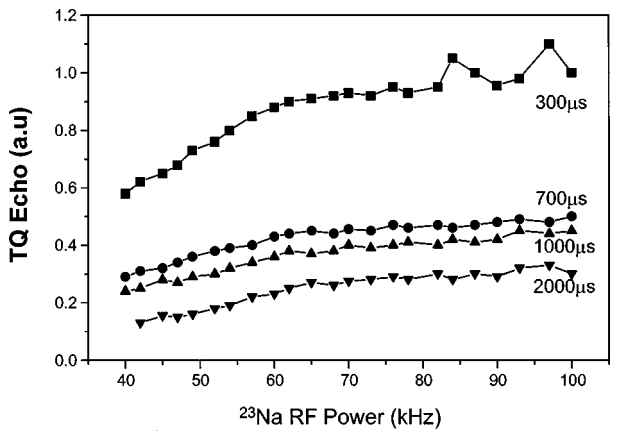

FIG. 14. Dependence observed for the ^{23}Na MQMAS echo intensity for Na_2SO_4 as a function of the rf power for various interpulse delays: $t_1 = 300$, 700, 1000, and 2000 μs. Data were collected using the acquisition parameters given in Fig. 12.

tion of the rf power employed for the modulation. In all these experiments the first pulse was always applied with a nutation rate of 104 kHz, while the strength of the modulated pulse was varied from 104 to 40 kHz. It is observed that the MQMAS FAM echo intensities remain fairly uniform down to fields of about 60 kHz, and only then do they start to decrease. We have also observed this feature in numerical simulations, and it is again reflecting the fact that efficiencies of adiabatic transfers are not crucially dependent on the strength of the rf. All these aspects are relevant when extending the ideas of FAM to higher spin systems like ^{17}O, characterized by large second-order quadrupolar couplings and relatively low γ values.

To conclude this section it may be worth noting that according to the experimental observations, the intensities of MQMAS echoes may be further enhanced by other, more elaborate FAM-based schemes. We have observed, for instance, that $Na_2C_2O_4$ MQMAS signals show a further 15% enhancement by changing the delay between pulses and the pulse widths in the modulation from a uniform 1 μs value to 0.3 and 0.8 μs, respectively. That this should result in a performance improvement is also corroborated by numerical simulations. But for all practical and routine purposes it suffices to set the various pulses and delays involved in the discrete FAM conversion pulse to equal values, and then optimize the duration of these levels and the number of times that the module is repeated for any given rf power. Additional precautions needed for MQMAS FAM experiments on higher spins will be discussed in a coming publication.[52]

IV. CONCLUSIONS

The principles and applications of new MQMAS methodologies have been analyzed here in detail within the framework of single transition operators and of adiabatic coherence transfer processes. These arguments enabled us to understand the various ways in which both cw or modulated pulses influences the conversion profiles in single crystal MQMAS experiments. The insights thus gained were also useful to get a more clear picture of the complex dynamics that characterizes the MQMAS echo formation with respect to the refocusing of precessing coherences in powders. These arguments on the formation of coherence echoes are actually quite general, and can be extended in a straightforward manner to the analysis of several other solid state NMR experiments such as REAPDOR and cross polarization transfers from and to quadrupolar spins. Such analyses are currently under way.

ACKNOWLEDGMENTS

The authors would like to thank the US–Israel Binational Science Foundation for funding this research. L.F. thanks the Weizmann Institute for a Meyerhoff Visiting Professorship (1998), as well as the U.S. National Science Foundation (DMR-9806810 and CHE-9841790) and the A.P. Sloan Foundation for support.

APPENDIX

In this Appendix we outline some properties of the fictitious spin $\frac{1}{2}$ operators that have been used in various sections. All these properties have been given in further detail by Vega[44] and we just reproduce here certain aspects that are relevant for this paper. The nonzero terms of the single transition operators I_x^{ij}, I_y^{ij}, and I_z^{ij} are defined as

$$\begin{aligned}
&\langle i|I_x^{ij}|j\rangle=\langle j|I_x^{ij}|i\rangle=\tfrac{1}{2},\\
&\langle i|I_y^{ij}|j\rangle=-\langle j|I_y^{ij}|i\rangle=-\frac{i}{2},\\
&\langle i|I_z^{ij}|j\rangle=-\langle j|I_z^{ij}|i\rangle=\tfrac{1}{2}.
\end{aligned} \tag{A1}$$

The following commuation relations have been used in arriving at Eqs. (10), (20), and (22). They have also been used to arrive at the results of the transformations given in Eqs. (26), (32), (42), (44), (46), and (48),

$$\begin{aligned}
&[I_x^{ij},I_y^{ij}]=iI_z^{ij},\\
&[I_x^{ij},I_x^{jk}]=\frac{i}{2}I_y^{ik},\\
&[I_y^{ij},I_y^{jk}]=-\frac{i}{2}I_y^{ik},\\
&[I_x^{ij},I_y^{jk}]=-\frac{i}{2}I_x^{ik},\\
&[I_z^{ij},I_z^{jk}]=0,\\
&[I_p^{ij},I_z^{ik}+I_z^{jk}]=0,\quad p=x,y.
\end{aligned} \tag{A2}$$

The first four of these commutation relations hold well for cyclic permutations of the three operators, *x*,*y*, and *z*.

The following commutation relations have been used in the transformation dealing with the discussion of adiabaticity:

$$\begin{aligned}
&[I_x^{12}+I_x^{34},I_y^{23}+I_y^{14}]=0,\\
&[I_z^{12}-I_z^{34},I_y^{23}-I_y^{14}]=0,\\
&[I_x^{12}+I_x^{34},I_x^{14}-I_x^{23}]=-i(I_y^{13}-I_y^{24}),\\
&[I_x^{12}+I_x^{34},I_y^{14}-I_y^{23}]=i(I_x^{13}-I_x^{24}).
\end{aligned} \tag{A3}$$

To arrive at Eq. (21) we use the fact that for a 2×2 matrix of the form $\exp(i(aI_x+bI_z))$ where *a* and *b* are any constants the evolution operator *U* can be written in the form

$$U=\exp(i\alpha I_y)\exp(i\sqrt{a^2+b^2}I_x)\exp(-i\alpha I_y), \tag{A4}$$

where

$$\tan\alpha=\frac{b}{a}. \tag{A5}$$

The following commutation relations are useful to calculate transformations of the form given in Eqs. (45) and (47).

$$
\begin{aligned}
&[I_y^{ij} \pm I_y^{kl}, I_y^{ik} \mp I_y^{jl}] = i(I_y^{il} \pm I_y^{jk}),\\
&[I_x^{ij} \pm I_x^{kl}, I_x^{ik} \mp I_x^{jl}] = i(I_y^{il} \mp I_y^{jk}),\\
&[I_x^{ij} \pm I_x^{kl}, I_y^{ik} \mp I_y^{jl}] = i(I_x^{il} \mp I_x^{jk}).
\end{aligned} \tag{A6}
$$

These commutation relations hold well for the cyclic permutations of the three sum operators. Equation (48) has been arrived at by making use of the first of commutation relations in Eq. (A6).

The transformation equations in this paper are based on the following convention. For U given by

$$U = \exp(i\theta A) \tag{A7}$$

the following holds well:

$$U^{-1}BU = \exp(-i\theta A)B\exp(i\theta A) = A\cos\theta + C\sin\theta, \tag{A8}$$

where we use the following definitions:

$$[A,B] = iC. \tag{A9}$$

As an example, using Eq. (A2) we can write

$$U_y^{ij}(-\theta)I_y^{jk}U_y^{ij}(\theta) = I_y^{jk}\cos\left(\frac{\theta}{2}\right) - I_y^{ik}\sin\left(\frac{\theta}{2}\right), \tag{A10}$$

where

$$U_p^{ij}(\theta) \equiv \exp(i\theta I_p^{ij}), \quad p = x,y,z. \tag{A11}$$

[1] G. E. Maciel, Science **226**, 282 (1984).
[2] E. Oldfield and R. J. Kirkpatrick, Science **227**, 1537 (1985).
[3] G. L. Turner, R. J. Kirkpatrick, S. H. Risbud, and E. Oldfield, Am. Ceram. Soc. Bull. **66**, 656 (1987).
[4] S. L. Gann, J. H. Baltisberger, E. W. Wooten, H. Zimmermann, and A. Pines, Bull. Magn. Reson. **16**, 68 (1994).
[5] C. A. Fyfe, K. C. Wong-Moon, Y. Huang, and J. Gondey, J. Am. Chem. Soc. **117**, 10397 (1995).
[6] *Solid State NMR of Inorganic Materials*, edited by J. J. Fitzgerald (American Chemical Society, Washington, DC, 1999), p. 917.
[7] L. Frydman and J. S. Harwood, J. Am. Chem. Soc. **117**, 5367 (1995).
[8] G. Wu, D. Rovnyak, P. C. Huang, and R. G. Griffin, Chem. Phys. Lett. **277**, 79 (1997).
[9] S. H. Wang, Z. Xu, J. H. Baltisberger, L. M. Bull, J. F. Stebbins, and A. Pines, Solid State Nucl. Magn. Reson. **8**, 1 (1997).
[10] P. J. Dirken, S. C. Kohn, M. E. Smith, and E. R. H. van Eck, Chem. Phys. Lett. **266**, 568 (1997).
[11] Z. Xu, H. Maekawa, J. V. Oglesby, and J. F. Stebbins, J. Am. Chem. Soc. **120**, 9894 (1998).
[12] L. Zuchner, J. C. C. Chan, W. Muller-Warmuth, and H. Eckert, J. Phys. Chem. B **102**, 4495 (1998).
[13] J. F. Stebbins and Z. Xu, Nature (London) **364**, 60 (1998).
[14] P. Sarv, B. Wichterlova, and J. Cejka, J. Phys. Chem. B **102**, 1372 (1998).
[15] S. R. Jansen, H. T. Hintzen, R. Metselaar, J. W. de Haan, L. J. M. van de Ven, A. P. M. Kentgens, and G. H. Nachtegaal, J. Phys. Chem. B **102**, 5969 (1998).
[16] S. J. Hwang, C. Fernandez, J. P. Amoureux, J. W. Han, J. Cho, S. W. Martin, and M. Pruski, J. Am. Chem. Soc. **120**, 7337 (1998).
[17] T. Charpeuntier and J. Virlet, Solid State Nucl. Magn. Reson. **122**, 227 (1998).
[18] A. Medek, J. S. Harwood, and L. Frydman, J. Am. Chem. Soc. **117**, 12779 (1995).
[19] C. Fernandez and J. P. Amoureux, Chem. Phys. Lett. **242**, 449 (1995).
[20] G. Wu, D. Rovnyak, B. Sun, and R. G. Griffin, Chem. Phys. Lett. **249**, 210 (1996).
[21] D. Massiot, B. Tonzo, D. Trumeau, J. P. Coutures, J. Virlet, P. Florian, and P. Grandinetti, Solid State Nucl. Magn. Reson. **6**, 73 (1996).
[22] J. P. Amoureux, C. Fernandez, and L. Frydman, Chem. Phys. Lett. **259**, 347 (1996).
[23] M. J. Duer and C. Stourton, J. Magn. Reson. **124**, 189 (1997).
[24] M. Hanaya and R. K. Harris, J. Phys. Chem. A **101**, 6903 (1997).
[25] J. P. Amoureux and C. Fernandez, Solid State Nucl. Magn. Reson. **10**, 211 (1998).
[26] J. P. Amoureux, C. Fernandez, and S. Steuernagel, J. Magn. Reson., Ser. A **123**, 116 (1996).
[27] S. P. Brown, S. J. Heyes, and S. Wimperis, J. Magn. Reson., Ser. A **119**, 280 (1996).
[28] D. Massiot, J. Magn. Reson., Ser. A **122**, 240 (1996).
[29] G. Wu, D. Rovnyak, and R. G. Griffin, J. Am. Chem. Soc. **118**, 9326 (1996).
[30] A. J. Vega, J. Magn. Reson. **96**, 50 (1992).
[31] J. P. Amoureux, M. Pruski, D. P. Lang, and C. Fernandez, J. Magn. Reson. **131**, 170 (1998).
[32] C. J. Lee, N. Murali, and W. S. Warren, Adv. Magn. Reson. **14**, 241 (1990).
[33] L. Marinelli, A. Medek, and L. Frydman, J. Magn. Reson. **132**, 88 (1998).
[34] S. Ding and C. A. McDowell, Chem. Phys. Lett. **270**, 81 (1997).
[35] S. Ding and C. A. McDowell, J. Magn. Reson. **132**, 88 (1998).
[36] S. Vega and Y. J. Naor, J. Chem. Phys. **75**, 75 (1981).
[37] A. P. M. Kentgens, J. Magn. Reson., Ser. A **95**, 619 (1991).
[38] J. Haase and M. S. Conradi, Chem. Phys. Lett. **287**, 2099 (1993).
[39] J. Haase, M. S. Conradi, C. P. Grey, and A. J. Vega, J. Magn. Reson., Ser. A **109**, 90 (1994).
[40] R. Fu, V. L. Emakov, and G. Bodenhausen, Solid State Nucl. Magn. Reson. **7**, 1 (1996).
[41] E. V. Veenednaal, B. H. Meier, and A. P. M. Kentgens, Mol. Phys. **93**, 195 (1998).
[42] A. P. M. Kentgens and R. Verhagen, Chem. Phys. Lett. **300**, 435 (1999).
[43] P. K. Madhu, A. Goldbourt, L. Frydman, and S. Vega, Chem. Phys. Lett. **307**, 41 (1999).
[44] S. Vega, J. Chem. Phys. **68**, 5518 (1978).
[45] A. Abragam, *Principles of Nuclear Magnetism* (Oxford University Press, Oxford, 1961).
[46] A. Messiah, *Quantum Mechanics* (North-Holland, Amsterdam, 1963), Vol. 2, p. 739.
[47] C. P. Grey, W. S. Veeman, and A. J. Vega, J. Chem. Phys. **98**, 7711 (1993).
[48] C. P. Grey and A. J. Vega, J. Am. Chem. Soc. **117**, 8232 (1995).
[49] T. Gullion, J. Magn. Reson., Ser. A **117**, 326 (1995).
[50] K. H. Lim and C. P. Grey, Solid State Nucl. Magn. Reson. **13**, 101 (1998).
[51] D. J. States, R. A. Haberkorn, and D. J. Ruben, J. Magn. Reson. **48**, 286 (1982).
[52] A. Goldbourt, P. K. Madhu, and S. Vega (unpublished).